APPLIED SCIENCES AND ENGINEERING

Ultrabright difuranfluoreno-dithiophen polymers for enhanced afterglow imaging of atherosclerotic plaques

Zhe Li[1]†, Hui Cao[1]†, Youjuan Wang[1], Shiyi Liao[1], Xu Li[1], Baode Chen[1], Xiaosha Wang[2], Lihui Jiang[2], Yingping Zou[2], Xiao-bing Zhang[1], Guosheng Song[1,3]*

Cardiovascular diseases, including stroke driven by atherosclerosis, remain a leading global health concern. Current diagnostic imaging modalities such as magnetic resonance imaging fail to characterize oxidative stress within atherosclerotic plaques. Here, we introduce difuranfluoreno-dithiophen–based polymers designed for afterglow imaging, offering ultrabright luminescence, ultralow-power excitation (0.087 milliwatts per square centimeter), and ultrashort acquisition times (0.01 seconds). Through a molecular engineering strategy, we have optimized polymers for enhanced reactive oxygen species (ROS) generation capability, ROS capturing capability, and fluorescence quantum yield, resulting in an increase in afterglow intensity (~130-fold) compared to commonly used 2-methoxy-5-(2′-ethylhexyloxy)-1,4-phenylenevinylene polymer (MEHPPV). Additionally, we have developed ratiometric afterglow nanoparticles doped with oxidative stress–responsive molecules, enabling imaging of oxidative stress markers in atherosclerotic plaque. This approach provides a tool for cardiovascular imaging and diagnostics, which is conducive to the auxiliary diagnosis and risk stratification of atherosclerosis.

INTRODUCTION

Cardiovascular diseases represent a global health challenge, ranking as leading causes of mortality and morbidity worldwide. Among these, stroke stands as the third leading cause of death, following closely behind cancer and ischemic heart disease (1–3). The underlying pathophysiology of stroke is frequently attributed to atherosclerosis, a condition predominantly resulting from the rupture of atherosclerotic plaques (4, 5). Differentiating between eroded and stable plaques is crucial for assessing plaque burden and vulnerability, which can guide the selection of appropriate pharmacotherapy for plaque stabilization, thereby improving patient outcomes (6). Moreover, research has established that both chronic and acute inflammation, leading to elevated levels of reactive species, plays a pivotal role in the development of atherosclerosis by promoting plaque instability and vulnerability (7, 8).

Despite advances in imaging modalities such as magnetic resonance imaging, positron emission tomography, and computed tomography, which can detect the presence and location of plaques, these techniques fall short in adequately reporting on oxidative stress and inflammation within plaques, particularly in the carotid artery (9–11). In recent years, the exploration of near-infrared fluorophores for imaging carotid atherosclerotic plaques has expanded, including agents like chlorin e6, indocyanine green, Bodipy, and aggregation-induced emission (AIE)–based organic dots (table S1) (12–21). However, their application in vivo has been limited because of the autofluorescence observed in living models. Afterglow luminescence, known for its long-persistent luminescence after the cessation of light excitation, emerges as an alternative by reducing autofluorescence and thereby enhancing the signal-to-background ratio (SBR) for more sensitive and accurate imaging (22–24). This technique has shown potential across various in vivo biomedical applications, such as imaging orthotopic

tumors in mice, detecting hepatotoxicity, imaging-guided surgery or therapy, and monitoring therapeutic process (25–31). Despite its promise, the development of afterglow probes specifically designed for assessing oxidative stress levels in plaques remains scarce, underscoring an urgent need in this area.

Historically, inorganic nanoparticles have been used to enhance afterglow luminescence; however, concerns regarding systemic toxicity due to potential heavy metal leakage have limited their application (32, 33). Organic afterglow nanoparticles, recognized for their biocompatibility and degradability, present a viable alternative (34–39). Yet, they are not without limitations, including lower photo-afterglow conversion efficiency, diminished luminescent intensity, required high-power laser excitation, extended acquisition times, and susceptibility to photobleaching during repeated imaging sessions (24, 40, 41). For instance, the use of high-power density laser excitation (1 W/cm² for an 808-nm laser), necessary for 2-methoxy-5-(2′-ethylhexyloxy)-1,4-phenylenevinylene polymer (MEHPPV)–based organic afterglow systems, poses risks of phototoxicity and tissue damage, which are concerns for safe clinical application (24, 42).

To address these challenges, we have developed the difuranfluoreno-dithiophen–based polymers capable of achieving ultrabright afterglow luminescence with ultralow-power excitation (0.087 mW/cm²) and ultrashort acquisition times (down to 0.01 s). This approach enhances the sensitivity, accuracy, and longevity of in vivo molecular imaging. By using a molecular engineering strategy, we systematically modulated the electron-deficient ability of the acceptor units within the polymers for enhanced reactive oxygen species (ROS) generation capability, ROS capturing capability, and fluorescence quantum yield (QY) (Fig. 1). This comprehensive strategy resulted in an enhancement of afterglow luminescence intensity, with our leading polymer nanoparticle formulation outperforming existing benchmarks (table S2) (22, 24, 28, 29, 31, 35, 40, 41, 43–50). Furthermore, we introduced ratiometric afterglow nanoparticles (RANPs) doped with oxidative stress–responsive molecules (ORM) for the precise quantification of oxidative stress markers. These RANPs demonstrated targeted affinity for plaque in vivo, enabling the imaging of intraplaque oxidative stress levels.

[1]State Key Laboratory of Chemo and Biosensing, College of Chemistry and Chemical Engineering, Hunan University, Changsha 410082, China. [2]College of Chemistry and Chemical Engineering, Central South University, Changsha 410083, China. [3]Shenzhen Research Institute, Hunan University, Shenzhen 518000, China.
*Corresponding author. Email: songgs@hnu.edu.cn
†These authors contributed equally to this work.
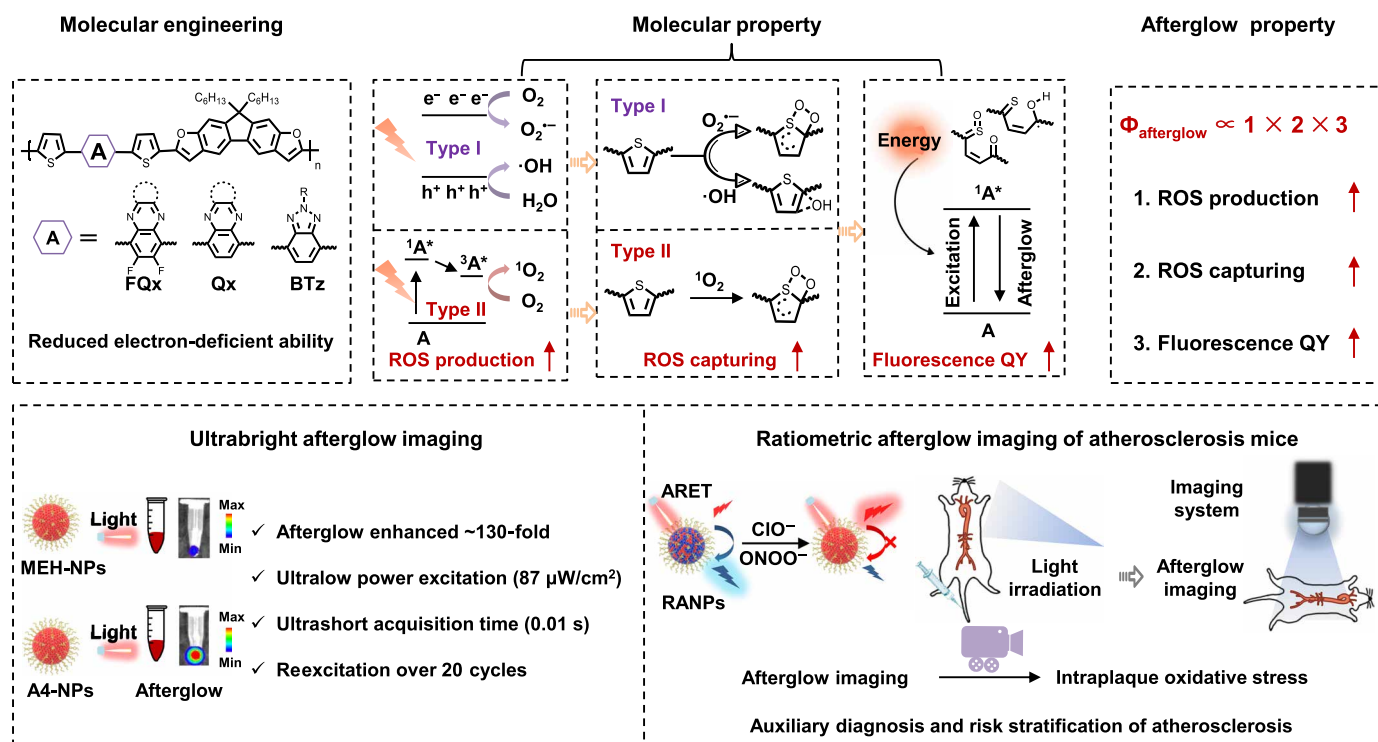
Fig. 1. Schematic illustration of molecular engineering, molecular property, afterglow property, afterglow imaging, and ratiometric afterglow imaging atherosclerosis mice. FQx, fluoro-quinoxaline; BTz, benzotriazole.

RESULTS

### Design and synthesis of afterglow semiconducting polymers

To address the need for advanced materials in afterglow luminescence imaging, we synthesized polymers by linking various acceptors (A) and donor (D) units. These included quinoxaline (Qx, M1), dithiophene-substituted quinoxaline (M2), dithiophene-substituted difluoroquinoxaline (M3), and dithiophene-substituted benzotriazole (DTBTz, M4) as the A units, alongside furan-fused fluorene (M5) as the D unit (Figs. 2 and 3A). The polymers A1, A2, A3, and A4 were formulated with these units, where A1 comprised a Qx A unit and a furan-fused fluorene D unit, while A2, A3, and A4 were composed of thiophene-substituted A units paired with the same D unit. The synthetic routes and characterization of the A1 through A4 polymers were detailed in Fig. 2 and figs. S1 to S13. The synthesis of M1, M2, and M3 units followed methodologies described in previous literature (*51*), while M4 and M5 units underwent a series of reactions starting from benzotriazole and 2,7-dihydroxy-9-fluorenone, respectively. The 2 was obtained by introducing 1-bromo-2-methylpropane, followed by the electrophilic substitution reaction of benzotriazole introducing two bromine atoms to obtain 3. Stille coupling reaction between 3 and tributyl (thiophen-2-yl)stannane produced 4, which was then synthesized by bromination reaction under *N*-bromosuccinimide condition to form M4. Starting with 2,7-dihydroxy-9-fluorenone (5), nucleophilic substitution reaction of 1-bromo-2,2-diethoxyethane and 5 produced 6. The 7 was synthesized by Wolff-Kishner-Huang-Minlon reduction reaction, and two hexyl chains were introduced into 7 to obtain 8. Intramolecular cyclization reaction in polyphosphoric acid condition produced 9. M5 was synthesized by substitution reaction between trimethyltin

chloride and 9. The desired polymers were synthesized by Stille coupling reaction between the corresponding brominated monomers (M1 to M4) and M5. The corresponding compounds were confirmed via ^{1}H nuclear magnetic resonance, aligning well with anticipated structures.

These polymers exhibited excellent solubility in common organic solvents such as tetrahydrofuran (THF), chloroform, and dichloromethane. We assessed their ultraviolet-visible (UV/vis) absorption and fluorescence spectra in THF solutions, noting that the A4 polymer displayed absorption shoulder peaks at 488 and 519 nm. Polymers A1, A2, and A3 exhibited a slight redshift of 18, 36, and 14 nm, respectively in absorption (fig. S15). The fluorescence emission spectra revealed that A1 and A4 showed a same maximum peak at approximately 596 nm, with A2 and A3 showing red shifts of 91 and 67 nm, respectively (fig. S15).

The polymers were processed into nanoparticles using nanoprecipitation with Pluronic-F127 as a surfactant, under consistent conditions (Fig. 3B). The A4-based nanoparticles (A4-NPs) were further examined using transmission electron microscopy and dynamic light scattering, revealing a hydrodynamic diameter of 80 to 90 nm and maintaining a spherical morphology with stable colloidal properties over 24 hours (Fig. 3C and fig. S16). UV/vis absorption and fluorescence spectra of these nanoparticles confirmed distinct absorption peaks at about 550, 558, 546, and 518 nm and maximum fluorescent emissions at about 610, 730, 720, and 620 nm, varying across the A1-NPs through A4-NPs (Fig. 3, D and E).

Afterglow luminescence was then quantified using an in vivo imaging system (IVIS) in bioluminescence mode. The thiophene-based nanoparticles (A2, A3, and A4) exhibited markedly stronger
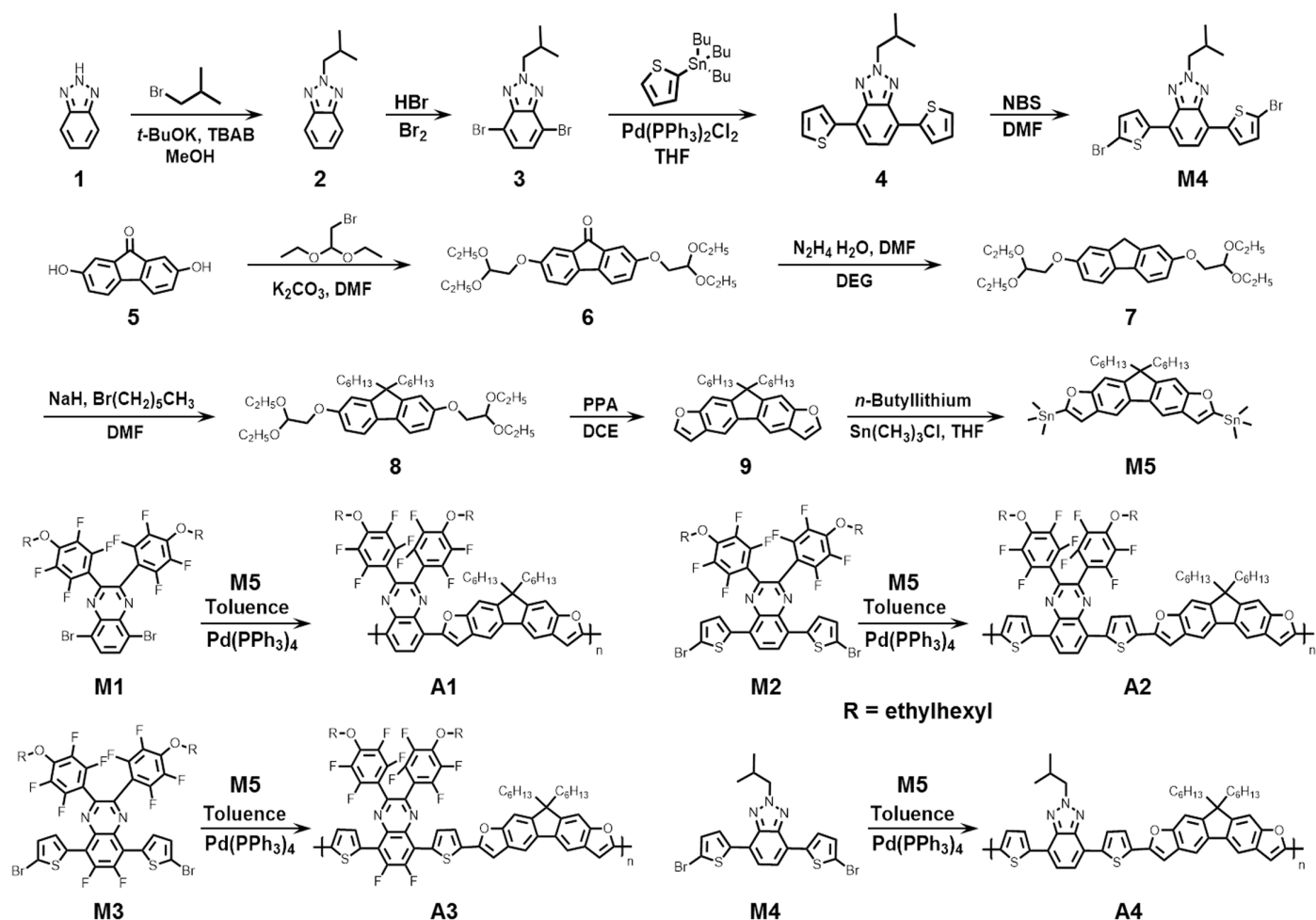
Fig. 2. Schematic illustration of polymers synthesis. MeOH, methanol; TBAB, tetrabutylammonium bromide; NBS, *N*-bromosuccinimide; DMF, *N,N'*-dimethylformamide; DEG, diethylene glycol; PPA, polyphosphoric acid; DCE, 1,2-dichloroethane.

afterglow luminescence compared to the thiophene-free A1, underscoring the critical role of thiophene in facilitating afterglow luminescence (Fig. 3, F and G). Notably, A4-NPs demonstrated a higher afterglow intensity than their counterparts, achieving an afterglow intensity approximately 576 times greater than that of A1-NPs and substantially surpassing A2-NPs and A3-NPs by approximately 55 and 260 times, respectively.

Afterglow luminescence mechanism

Previous research has highlighted that elevated afterglow intensity in organic materials is contingent upon three critical factors: high production of singlet oxygen $\left(^1O_2\right)$, efficient capturing of $^1O_2$, and high fluorescence efficiency (*22, 52*). To elucidate the mechanisms underlying increased afterglow intensity, we embarked on a comprehensive study, examining the ROS generation capability, ROS capturing capability, and fluorescence quantum yield (Fig. 4A).

For ROS generation capability, we firstly demonstrated the types of generated ROS under illumination and further evaluated the total ROS generation capacity. We used singlet oxygen sensor green (SOSG) as indicators to measure $^1O_2$ production of polymer-based nanoparticles. Light irradiation increased SOSG fluorescence intensity at 530 nm, indicating $^1O_2$ generation (fig. S17). The polymer-

based nanoparticles exhibited the increased fluorescence intensity, confirming the $^1O_2$ generation (fig. S16). The A4-NPs showed the highest $^1O_2$ generation among polymers (Fig. 4B). Next, we tested the •OH and $O_2^{\bullet-}$ generation by electron spin resonance (ESR) spectra, using 3,4-dihydro-2,2-dimethyl-2H-pyrrole *N*-oxide (DMPO) as indicators. In the presence of both DMPO and nanoparticles under light irradiation, the typical resonance peak for DMPO-•OH adducts (1:2:2:1) and DMPO-$O_2^{\bullet-}$ adducts (1:1:1:1) were observed, confirming the generation of •OH and $O_2^{\bullet-}$ based on polymer nanoparticles (Fig. 4, C and D). Subsequently, total ROS generation ability was evaluated by using 1.3-diphenylisobenzofuran (DPBF) as a ROS indicator. We calculated the ROS generation capacity by calculating the DPBF degradation percentage (the calculation formula of ROS generation capacity is in the "ROS generation capability" section of the Supplementary Materials). These corresponding values of formula were obtained from fig. S18 and shown in table S3. By substituting these values into calculation formula of ROS generation capacity, the calculated ROS generation capacity of A1-NPs, A2-NPs, A3-NPs, and A4-NPs were 20.80, 16.32, 14.74, and 33.29%, respectively. The results showed that A4-NPs had the highest ROS generation capability (Fig. 4E).

To analyze the reasons for the highly $^1O_2$ generation, we calculated the singlet-triplet energy gap (ΔE_{ST}) by density functional
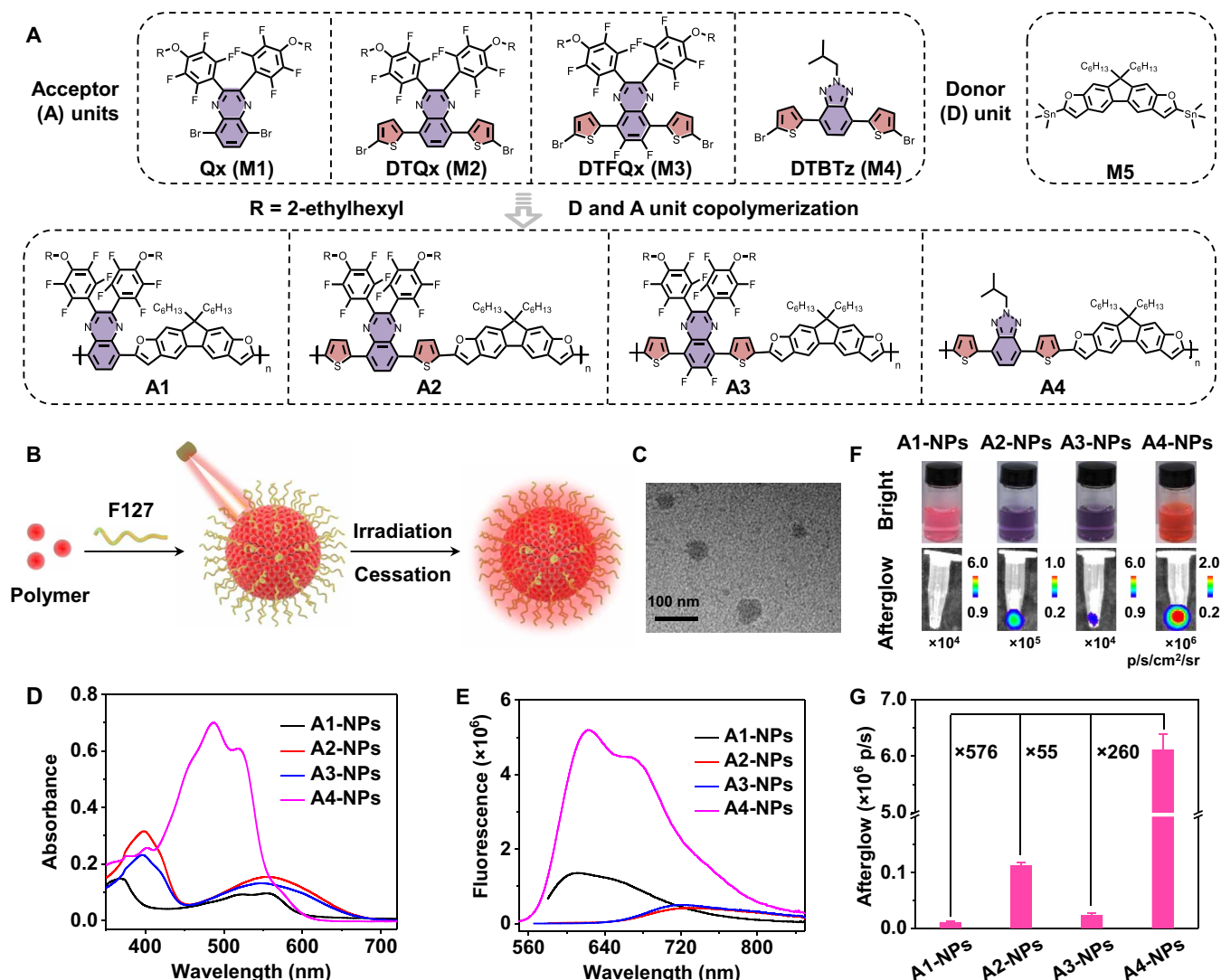
Fig. 3. Characterization of nanoparticles. (**A**) Molecular structures of acceptors, donor, and polymers. (**B**) Illustration of nanoparticle preparation via nanoprecipitation. (**C**) Transmission electron microscope of A4-NPs. (**D**) The absorption spectra and (**E**) fluorescence spectra of four nanoparticles. (**F**) Photographs (top) and afterglow images (bottom) of nanoparticles. (**G**) Quantification of afterglow intensities of nanoparticles in (F) (*n* = 3). Data are shown as mean ± SD. DTQx, dithiophene-substituted quinoxaline; DTFQx, dithiophene-substituted difluoroquinoxaline; DTBTz, dithiophene-substituted benzotriazole.

theory (DFT) calculations. The polymer structures are simplified to a monomer polymer with a polymerization degree of one. The small ΔE_{ST} promoted the intersystem crossing efficiency and further improved the $^1O_2$ generation (*53*). The calculated ΔE_{ST} for monomer polymers A1, A2, A3, and A4 were 0.97, 0.97, 0.86, and 0.20 eV, respectively (Fig. 4F). Compared to A1 to A3 monomer polymers, the A4 monomer polymer owned the smallest ΔE_{ST}, which was consistent with the highest $^1O_2$ generation of A4-NPs. The A2 and A3 monomer polymers show small deviation between ΔE_{ST} and $^1O_2$ generation, due to deviations between the theoretical calculations based on simplified polymers and actual testing based on polymer-based nanoparticles. In addition, to analyze the reasons for the highly •OH and $O_2^{•-}$ generation, we investigated the photocurrent generation of polymers. The high photocurrents indicated high photoexcited electrons and holes, which was conducive to produce $O_2^{•-}$ and •OH, respectively (*54*, *55*). For measuring photocurrents, the devices

based on the polymers was fabricated by the spin coating method and showed in Fig. 4G. After light irradiation, the devices based on the A4 polymer showed the highest photocurrents among polymers, which was consistent with the high •OH and $O_2^{•-}$ generation of A4-NPs (Fig. 4H).

For ROS capturing capability, the polymers could be degraded by ROS, resulting in decrease of fluorescence intensity (*56*). Furthermore, the ROS capturing capability was calculated by calculating the fluorescence decrease percentage of polymer-based nanoparticles after addition of ROS (the calculation formula of ROS capturing capability is in the "ROS capturing capability" section of the Supplementary Materials). These corresponding values of formula were obtained from fig. S19 and shown in table S4. For A1-NPs, it showed almost zero capturing capacity of $^1O_2$, •OH, and $O_2^{•-}$, due to the lack of thiophene units as ROS capturing unit (Fig. 4I). For A2-NPs and A3-NPs, they showed the higher $^1O_2$, •OH, and $O_2^{•-}$ capturing
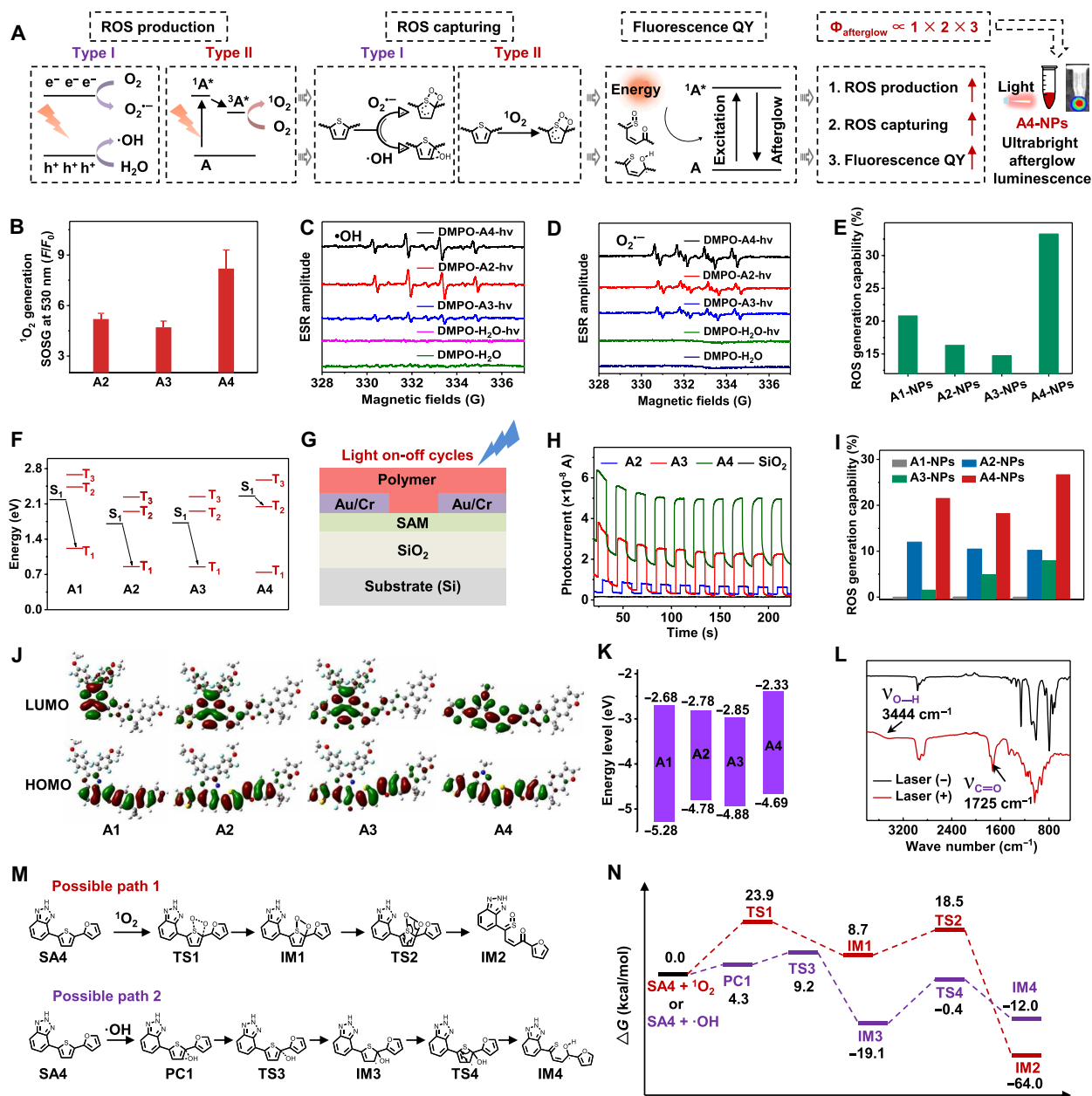
Fig. 4. Afterglow luminescence mechanism. (**A**) General schematic illustration of afterglow luminescence mechanism. (**B**) $^1O_2$ generation capacity of various nanoparticles with light irradiation (12 mW/cm^2) for 60 s ($n = 3$). The production of (**C**) •OH and (**D**) $O_2^{•-}$ by ESR. (**E**) The ROS generation capability of polymers under irradiation (4 W/cm^2, 10 s). (**F**) DFT calculation of polymers energy levels of excited single state (S_1) and excited triplet state (T_n). (**G**) Device structure of testing photocurrent. (**H**) Photocurrent responses (light on/off cycle: 20 s; duty cycle: 50%). (**I**) $^1O_2$, •OH, and $O_2^{•-}$ capturing capability of polymer. (**J**) DFT calculation of polymers HOMO and LUMO energy levels. (**K**) Quantification of energy levels of polymers in (J). (**L**) FTIR spectra of A4 before and after irradiation. (**M**) DFT calculation for reaction pathways of A4 with ROS. (**N**) Energy values of corresponding structure and transition state. Data are shown as mean ± SD.

capacity (around 2 to 12%), compared with A1-NPs. For A4-NPs, it showed the highest $^1O_2$, •OH, and $O_2^{•-}$ capturing capacity (around 20%) among polymers (Fig. 4I). The results indicated that A4-NPs owned the highest ROS capturing capability, and A1-NPs owned the lowest ROS capturing capability due to the absence of thiophene units.

To further validate the role of thiophene units, we synthesized a polymer, A5, from which thiophene units were removed from the

A4 structure (figs. S14 and S20B). We then measured the afterglow luminescence of A5-NPs under identical conditions to A4-NPs. The A5-NPs exhibited luminescence near the background level, which were similar to A1-NPs (the absence of thiophene groups in A1-NPs, resulting in a background signal) (fig. S20, A to D). Meanwhile, the A4-NPs showed afterglow intensity 319 times greater than A5-NPs (fig. S20E). This stark contrast underscores the indispensable

role of thiophene moieties in facilitating robust afterglow luminescence.

To analyze the reasons for the highly $^1O_2$, •OH, and $O_2{}^{•-}$ capturing, we calculated the highest occupied molecular orbital (HOMO) levels of monomer polymers (A1 to A4) by DFT calculations. The HOMO picture and energy values were shown in Fig. 4 (J and K). The A4 monomer polymer showed the highest HOMO levels (−4.69 eV), and the A1 monomer polymer showed the lowest HOMO levels (−5.28 eV). A high HOMO made the polymer more easily oxidized, thus promoting the ROS capturing (*57*). Hence, the A4-NPs obtained the highest ROS capturing capability.

To further understand the reaction process between ROS and A4 polymer, we analyzed the effects of light-induced ROS production on the A4 polymer through absorption, fluorescence, and Fourier transform infrared (FTIR) spectra. The FTIR spectra indicated the appearance of carbonyl peak (1725 cm^{-1}) and hydroxyl peak (3444 cm^{-1}) after long-term light irradiation, suggesting the oxidation of thiophene units (Fig. 4L). The oxidation of thiophene units could lead to the destruction of the polymer skeleton, thereby reducing the absorption and fluorescence intensity of the polymer. Meanwhile, we tested the absorption and fluorescence spectra after long-term light irradiation. The result showed the reduced absorption and fluorescence spectra after light irradiation (fig. S21). Hence, we proposed the possible reaction paths between ROS and A4 by DFT calculations. The calculated structure of A4 was simplified with benzotriazole-furan–substituted thiophene (SA4). Because of the similar transition states experienced by $^1O_2$ and $O_2{}^{•-}$ in the reaction with aromatic hydrocarbons, we only calculated the reaction between $^1O_2$, •OH, and SA4 (*56*, *58*–*60*). The possible paths and corresponding energy were showed in Fig. 4 (M and N). The calculations revealed that $^1O_2$ could oxidize the S—C bond of thiophene through a π^2-π^2 cycloaddition reaction, leading to the formation of unstable intermediates (IM1), which then underwent O—O bond cleavage to form carbonyl derivatives (IM2) (*56*, *61*). Similarly, •OH was shown to add to the α-C and β-C of thiophene, forming reactive intermediates (PC1) (*58*). PC1 could transform to IM3 via attacking α-C of thiophene. Next, S—C bond was broken to form IM4.

For fluorescence quantum yield (QY), we measured QY of polymer-based nanoparticles, using rhodamine B as a reference (QY = 65% in ethanol) (the calculation formula of QY is in the "Fluorescence quantum yield" section of the Supplementary Materials) (*62*, *63*). These corresponding values of formula were obtained from fig. S22 and shown in table S5. The QY values of polymer-based nanoparticles were 83.66% for A1-NPs, 5.16% for A2-NPs, 5.20% for A3-NPs, and 75.43% for A4-NPs, respectively. The results indicated that A1-NPs and A4-NPs owned the higher fluorescence quantum yield compared with A2-NPs and A3-NPs. To better elucidate the high quantum yield of A1-NPs and A4-NPs, we calculated the radiative and nonradiative rates (k_r and k_{nr}) and k_r/k_{nr} of nanoparticles (the calculation formula of rates is in the "Radiative and nonradiative rates" section of the Supplementary Materials). These corresponding values of formula were obtained from fig. S23 and table S5 and shown in table S6. The result showed that A4-NPs owned the 20-fold higher k_r (0.45) and a 2-fold lower k_{nr} (0.15) compared to A2-NPs and A3-NPs. These numbers favor the radiative rate while suppressing nonradiative rate, jointly enhancing the fluorescence quantum yield of A4-NPs. For A1-NPs, although A1-NPs have a 4-fold lower k_r than A4-NPs, it also exhibits a lower k_{nr} by 7-fold, resulting in a 1.7-fold higher k_r/k_{nr} ratio. This suggests that nonradiative

processes are markedly suppressed in A1-NPs, contributing to the highest fluorescence quantum yield among the tested polymers. For the polymer structure, compared to A2 to A4 polymers, the A1 had no thiophene units, which avoided the rotation between the thiophene and other units in polymers. The decreased rotation of the A1 polymer was conducive to reducing energy loss, leading to low k_{nr} and high fluorescence quantum yield. Meanwhile, we calculated the oscillator strength of the monomer polymers A1 to A4 by DFT calculations (table S7).

Together, the afterglow intensity of organic materials was proportional to three critical factors: ROS generation capability, ROS capturing capability, and fluorescence quantum yields (table S8). To enhance afterglow luminescence, synergistic improvement of these three factors was essential. Therefore, we further analyzed these factors and presented their values in table S8. For ROS generation capability, A4-NPs owned the highest ROS generation capability. The A2-NPs and A3-NPs owned the lower ROS generation capability compared with A1-NPs and A4-NPs. For ROS capturing capability, A4-NPs owned the highest $^1O_2$, $O_2{}^{•-}$ and •OH capturing capability among polymers. The A1-NPs owned the lowest $^1O_2$, $O_2{}^{•-}$ and •OH capturing capability (around 0%) due to the absence of thiophene as a ROS capturing unit. For fluorescence quantum yield, A4-NPs and A1-NPs owned the higher around 15-fold quantum yields compared with A2-NPs and A3-NPs. Hence, the A4-NPs achieved the highest afterglow luminescence, due to the highest ROS generation capability, the highest ROS capture capability, and the higher QY among polymers. The A1-NPs obtained the lowest afterglow luminescence, due to the absence of thiophene as a ROS capturing unit, resulting in a zero ROS capturing. Compared to A3-NPs, the A2-NPs had a slightly stronger afterglow than A3-NPs, due to A2-NPs exhibiting higher ROS generation capability and higher ROS capture capability at similar QY values. These results demonstrated that A4-NPs achieved the highest afterglow intensity by simultaneously improving ROS generation capability, ROS capturing capability, and fluorescence QY.

Optimization of afterglow performance in A4-NPs
To enhance afterglow imaging capabilities, we focused on optimizing the afterglow performance of A4-NPs, selected for their superior luminescence intensity. When compared under identical conditions to traditionally used organic afterglow polymers, such as MEHPPV and poly[2,7-(9,9-di-octyl-fluorene)-alt-4,7-bis(thiophen-2-yl)benzo-2,1,3-thiadiazole] (PFODBT) (*24*, *56*), A4-NPs demonstrated higher afterglow intensity—approximately 130 times greater than MEHPPV-based nanoparticles (MEH-NPs) and 169 times that of PFODBT-based nanoparticles (PFO-NPs) (Fig. 5, A to C). This remarkable efficiency in afterglow luminescence not only augments the efficacy of excitation but also enables the use of ultralow-power light sources for excitation, including mobile phone flashlights and room light, thereby mitigating the risk of photo-induced tissue damage.

Further investigation into the afterglow luminescence of A4-NPs across various excitation powers (white light: 12, 0.78, and 0.087 mW/cm^2) and acquisition times (10, 1, and 0.01 s), A4-NPs produced a strong afterglow signal even under room light (0.087 mW/cm^2) or an acquisition time of 0.01 s (Fig. 5, D to G). In contrast, PFO-NPs displayed negligible afterglow under the same conditions. This capability to maintain high luminescence intensity with ultralow-power excitation (0.087 mW/cm^2) and short acquisition times (0.01 s) minimizes the chemical decomposition of the afterglow polymers,
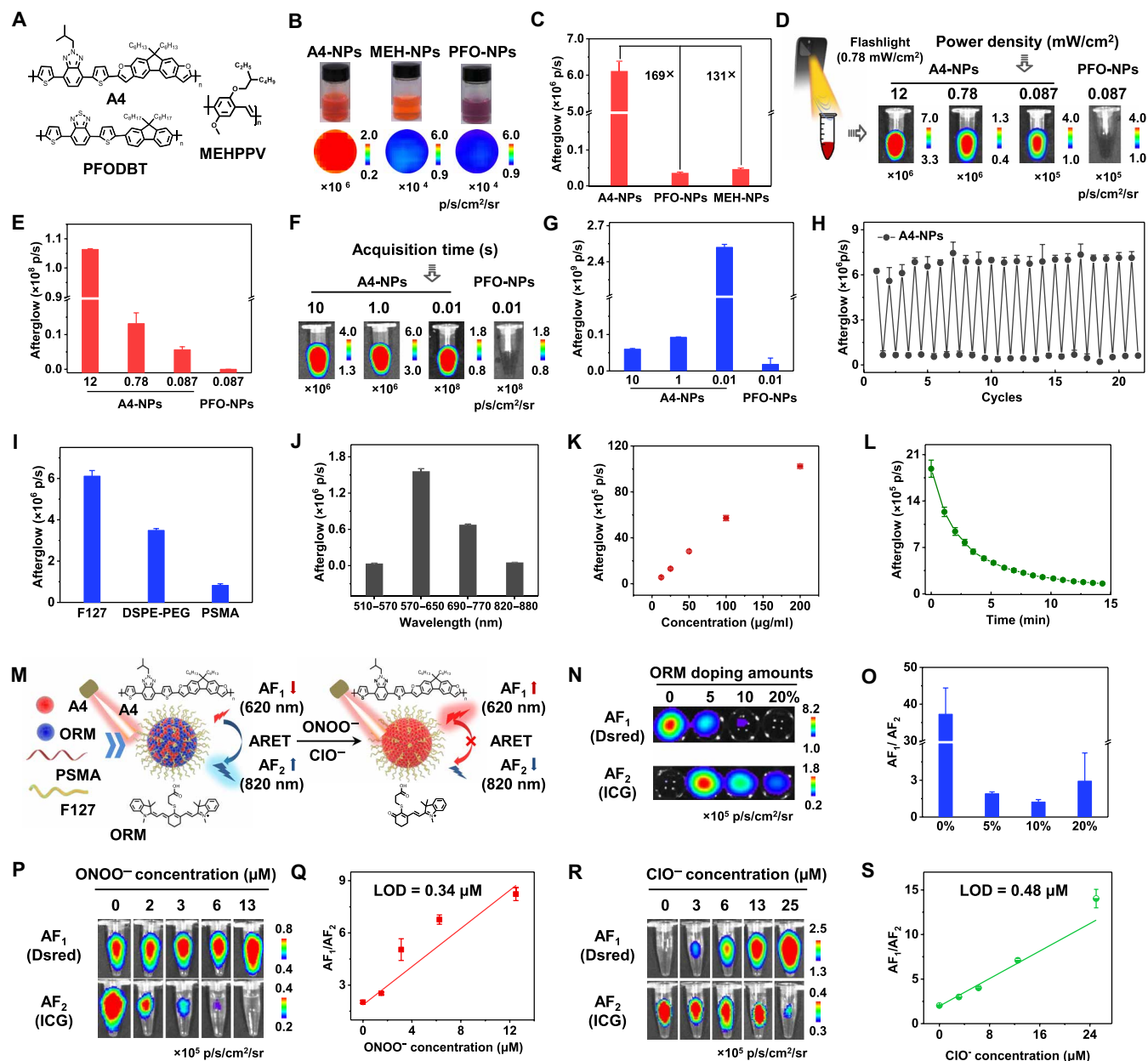
Fig. 5. Optimization afterglow performance of A4-baesd nanoparticles. (**A**) Chemical structures of A4, PFODBT, and MEHPPV. (**B**) Afterglow intensity of A4-NPs, PFO-NPs, and MEH-NPs with white light (12 mW/cm^2) for 20 s. (**C**) Quantification of afterglow intensity in (B) ($n = 3$). (**D**) Afterglow intensities in different power density (12, 0.78, and 0.087 mW/cm^2) for 20 s. (**E**) Quantification of afterglow intensities in (D) ($n = 3$). (**F**) Afterglow intensities with different acquisition time (12 mW/cm^2). (**G**) Quantification of afterglow intensities in (F) ($n = 3$). (**H**) Afterglow reexcitation cycles of A4-NPs with white light (0.087 mW/cm^2) for 20 s ($n = 3$). (**I**) Afterglow intensities of A4-NPs in different surfactants with white light (12 mW/cm^2) for 20 s ($n = 3$). (**J**) Afterglow emission of A4-NPs in GFP (510 to 570 nm), Dsred (570 to 650 nm), Cy5.5 (690 to 770 nm), and ICG (820 to 880 nm) channels with white light (12 mW/cm^2) for 20 s ($n = 3$). (**K**) Afterglow intensities of A4-NPs with different concentrations with white light (12 mW/cm^2) for 20 s ($n = 3$). (**L**) The dynamics of afterglow luminescence of A4-NPs with white light (12 mW/cm^2) for 20 s ($n = 3$). (**M**) Schematic illustration of ratiometric afterglow sensing. (**N**) Afterglow imaging of RANPs with different ORM doping amounts with white light (12 mW/cm^2) for 20 s. (**O**) Quantification of AF1/AF2 values in (N) ($n = 3$). (**P**) Afterglow imaging of RANPs upon activation of ONOO$^-$ with white light (12 mW/cm^2) for 20 s. (**Q**) The linear relationship of RANPs and ONOO$^-$ ($n = 3$). (**R**) Afterglow imaging of RANPs upon activation of ClO$^-$ with white light (12 mW/cm^2) for 20 s. (**S**) The linear relationship of RANPs and ClO$^-$ ($n = 3$). Data are shown as mean ± SD. LOD, limit of detection.

enhancing the durability of the imaging process. Upon reexcitation, the afterglow signals of A4-NPs maintained their maximum intensity without observable decay over more than 20 cycles (Fig. 5H), showcasing exceptional stability and reliability for repeated and dynamic molecular imaging applications.

In our systematic optimization efforts, we explored various surfactants to improve afterglow luminescence, with Pluronic F-127, distearoyl phosphoethanolamine–poly(ethylene glycol) 2000, and styrene maleic anhydride copolymer (PSMA) being evaluated. F-127 emerged as the optimal choice, enhancing the ROS generation, ROS

capture, and fluorescence efficiency and thereby increasing the afterglow intensity of A4-NPs (Fig. 5I and fig. S25). Spectral analysis across different emission channels revealed that A4-NPs exhibited their strongest luminescence in the 570- to 650-nm range, with intensity increasing alongside nanoparticle concentration and irradiation time (Fig. 5, J and K, and fig. S26).

Long-term afterglow luminescence dynamics were assessed by continuously acquiring images. The results highlighted A4-NPs' capability to sustain luminescence with a half-life of approximately 2 min, persisting for more than 14 min postirradiation cessation (Fig. 5L).

To create responsive afterglow probes, we doped A4-NPs with an ORM, forming RANPs capable of assessing oxidative stress levels through afterglow resonance energy transfer (Fig. 5M). This process allows for the precise quantification of oxidative stress markers by measuring the ratio of two emission signals (AF_1/AF_2). Optimization of ORM doping levels was conducted to achieve efficient energy transfer from A4 to ORM (Fig. 5, N and O). Considering both the afterglow signal intensity of AF_2 and AF_1/AF_2 values, the 5% doping level was chosen as optimal for subsequent imaging experiments.

The response of RANPs to increasing concentrations of $ONOO^-$ and ClO^- was thoroughly analyzed, demonstrating a linear relationship between the concentration of these oxidative stress markers and the AF_1/AF_2 ratio of afterglow signals (Fig. 5, P to S). This linear relationship, coupled with the calculated limits of detection (0.34 μM for $ONOO^-$ and 0.48 μM for ClO^-), confirms the efficacy of RANPs in quantitatively measuring oxidative stress levels. Thus, through meticulous optimization and innovative design, we have developed a highly sensitive and stable afterglow imaging system capable of precisely quantifying oxidative stress markers.

In vivo afterglow imaging performance

The remarkable afterglow performance of A4-NPs prompted an investigation into their imaging penetration depth and the SBR. Samples of A4-NPs, preirradiated with white light (12 mW/cm²) for 20 s, were overlaid with chicken tissues of varying thicknesses (4, 8, 10, 18, and 22 mm), and their afterglow images were subsequently captured. The results demonstrated that the afterglow imaging could discern luminescent signals through 22 mm of chicken breast tissue, in contrast to fluorescence imaging, which failed to produce visible signals in 18 mm of tissue coverage (Fig. 6A). This finding indicates a notable enhancement in penetration depth for afterglow imaging. Moreover, the SBR of afterglow imaging was found to be 67-fold higher than that of fluorescence imaging with 18-mm covering tissue, suggesting that A4-NPs offer potential for high SBR and deep tissue imaging in vivo (Fig. 6B).

To further assess the in vivo imaging feasibility of A4-NPs, subcutaneous afterglow imaging was performed. Initially, the afterglow luminescence performance of A4-NPs under varying excitation powers was evaluated. Following the subcutaneous injection of A4-NPs into mice, different levels of power irradiation (12, 0.78, and 0.087 mW/cm²) were applied. The afterglow luminescence signals were immediately captured using an IVIS imaging system. Robust afterglow luminescence signals were observed in the injection areas of the mice, with signals still evident under the lower excitation powers of 0.78 and 0.087 mW/cm², underscoring the exceptional photoexcitation efficiency of A4-NPs (Fig. 6, C to E, and fig. S27).
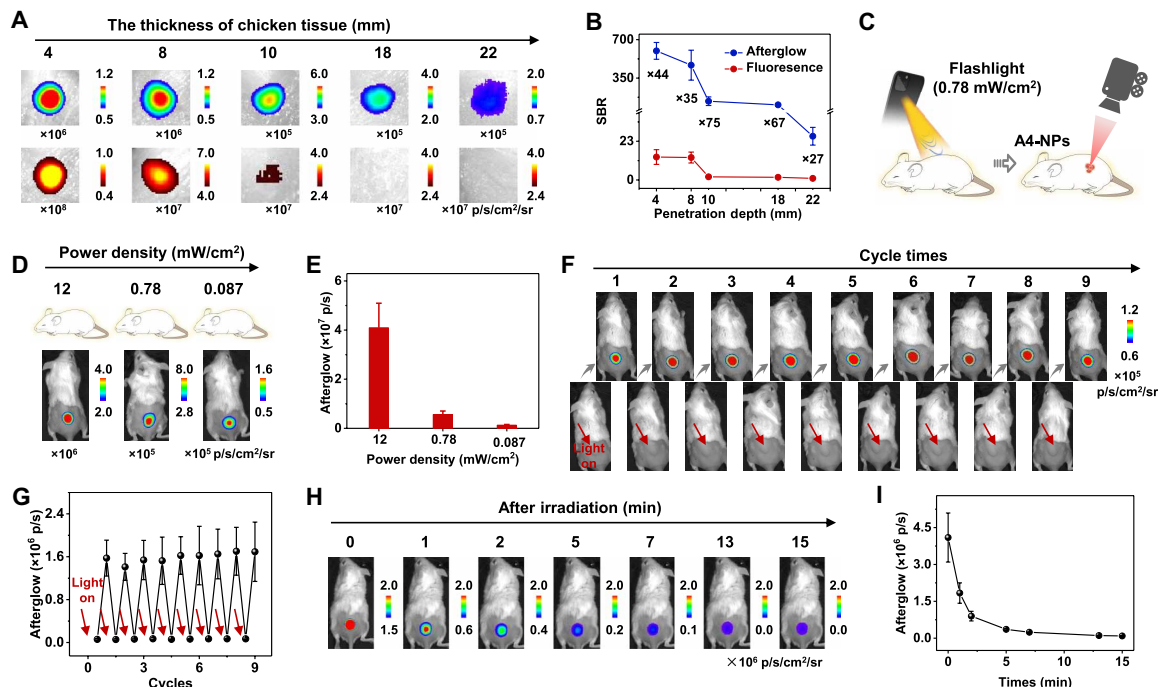
Fig. 6. Afterglow imaging performance in tissue or in vivo. (**A**) Penetration depth covered by different thickness of chicken breast tissues based on afterglow imaging (top) and fluorescence imaging (bottom). (**B**) SBR for afterglow and fluorescence from (A) ($n = 3$). (**C**) Schematic diagram of afterglow imaging of mice stimulated by mobile phone light. (**D**) Afterglow imaging of mice with subcutaneous injection. Those mice were preirradiated by different power light (12, 0.78, and 0.087 mW/cm²) for 20 s. (**E**) Quantification of afterglow intensities in (D) ($n = 3$). (**F**) Afterglow reexcitation cycles of mice with power (0.087 mW/cm²) for 20 s. (**G**) Quantification of afterglow intensities in (F) ($n = 3$). (**H**) Afterglow dynamic imaging of mice with white light (12 mW/cm²) for 20 s. (**I**) Quantification of afterglow intensities in (H) ($n = 3$). Data are shown as mean ± SD.

Given the superior afterglow performance at ultralow-power light excitation, the reexcitation cycles of A4-NPs in subcutaneously injected mice were examined. Mice were subjected to multiple irradiations with ultralow-power light (0.087 mW/cm^2), with each irradiation followed by a period allowing for photon release about 10 min before the next. Notably, distinct afterglow signals were observed after each irradiation, with no obvious reduction in signal intensity across 9 cycles (Fig. 6, F and G). This reexcitation performance suggests that A4-NPs can facilitate the quantification of afterglow signals during repeated imaging sessions.

In addition, the dynamics of afterglow luminescence following the cessation of irradiation were explored. Mice injected subcutaneously with A4-NPs underwent irradiation at 12 mW/cm^2 for 20 s, with luminescence signals captured through continuous afterglow imaging. The dynamic imaging revealed persistent luminescence exceeding 15 min postirradiation (Fig. 6, H and I).

Last, biodistribution experiments were conducted to elucidate the in vivo distribution pattern of A4-NPs. Mice intravenously injected with A4-NPs (2 mg/ml, 200 μl) were euthanized at 1 and 24 hours postinjection, and major organs were collected for afterglow imaging. The imaging results indicated a relatively strong signal presence in the liver, intestines, and lungs at both time points (fig. S28).

Afterglow imaging for assessing oxidative stress in atherosclerotic plaque in mouse model

Vascular dysfunction resulting from atherosclerosis (AS) contributes to the global burden of severe health issues, including high mortality and morbidity rates (1–3). Systematic inflammation exacerbates the condition by increasing inflammatory cell activity, which in turn elevates oxidative stress plaques, leading to enhanced recruitment of macrophages and neutrophils (64–68). This process is characterized by the activation of neutrophils due to oxidative stress, resulting in the overexpression of myeloperoxidase that produces hypochlorous acid (ClO$^-$) (15, 69). Concurrently, macrophages respond to oxidized low-density lipoprotein by expressing inducible nitric oxide (NO) synthase, which catalyzes the production of NO. This NO reacts with superoxide anions to form peroxynitrite (ONOO$^-$), further exacerbating oxidative stress within the plaque (70, 71). This increased oxidative stress level facilitates the transition from stable to vulnerable plaques (72–74). To address this issue, we introduce RANPs for imaging intraplaque oxidative stress in AS mouse models through afterglow imaging.

To induce atherosclerotic plaque formation in a mouse model, apolipoprotein E knockout (ApoE$^{-/-}$) male mice were subjected to left carotid artery ligation, followed by high-fat feeding for 12 weeks (Fig. 7A). Subsequent measurements of blood cholesterol levels in these ApoE$^{-/-}$ mice, compared to healthy controls, revealed a 28-fold increase, indicating sufficiently high to drive atherosclerosis (Fig. 7B). In addition, hematoxylin and eosin (H&E) staining confirmed the presence of plaques, confirming the successful establishment of the AS model (fig. S29).

To accelerate the process of arteriosclerosis, lipopolysaccharide (LPS) was used to elevate systemic inflammation levels. Atherosclerotic mice were subjected to nasal administration of LPS on three occasions (Fig. 7A) (19). Subsequently, we quantified white blood cell (WBC) counts in mouse blood samples and conducted H&E staining of lung tissues to evaluate the inflammation levels in AS mice treated with LPS. As depicted in Fig. 7C, an elevation in WBC

counts was observed in AS mice treated with LPS compared to AS mice alone (**$P = 0.0031$). Post-LPS administration, H&E staining of lung tissues revealed the presence of severe inflammation (fig. S30).

Following this, we used RANPs for afterglow imaging to assess the oxidative stress levels in carotid plaque among AS mice and those with LPS treatment. Groups of AS mice and AS mice with LPS treatment ($n = 5$ per group) were intravenously injected with RANPs (2.0 mg/ml, 200 μl). These mice were then exposed to white light irradiation (30 mW/cm^2) for 20 s on the left carotid artery. Subsequent afterglow imaging was performed, capturing afterglow signals via the AF$_1$ (Dsred) and AF$_2$ [indocyanine green (ICG)] channels at various time points (1, 2, and 3 hours) postinjection.

The accumulation of RANPs in the plaque led to an increase in both AF$_1$ and AF$_2$ signals. Specifically, RANPs, upon interaction with ONOO$^-$ and ClO$^-$ within the plaque, resulted in an enhanced AF$_1$ signal while diminishing the AF$_2$ signal. Afterglow images indicated that the AF$_1$ signal gradually intensified, stabilizing approximately 2 to 3 hours postinjection (Fig. 7, D and E). Conversely, the AF$_2$ signal initially increased and then exhibited a gradual decline (Fig. 7F). The augmentation of AF$_1$ signals could be attributed to RANP accumulation and their response to oxidative stress, which concurrently activated AF$_1$ signals within the plaque. The observed changes in AF$_2$ signals were due to the initial boost followed by a deactivation over time, also in response to oxidative stress, leading to a progressive reduction. Notably, the ratio of AF$_1$/AF$_2$ signals increased over time (Fig. 7G) for AS mice with LPS treatment, demonstrating higher ratios than AS mice at 3 hours postinjection (*$P = 0.0414$), indicative of elevated oxidative stress levels.

To further corroborate the oxidative stress levels within the plaques, carotid arteries were harvested from euthanized mice. These samples were stained with 2′,7′-dichlorofluorescin diacetate (DCFH-DA), a recognized ROS indicator. Confocal fluorescence imaging revealed that the fluorescence intensity of carotid plaques in the AS mice with the LPS treatment group was higher compared to that in AS mice (Fig. 7H), aligning with the in vivo afterglow imaging findings and confirming the capability of RANPs to reflect oxidative stress within plaques.

In addition, we analyzed macrophage and neutrophil infiltration in the carotid plaque ex vivo through immunofluorescence staining. Applying anti-F4/80 and anti-Ly6G antibodies—markers for macrophages and neutrophils, respectively—revealed that the mean fluorescence intensity of carotid plaques in the AS mice with the LPS treatment group was 2.2 and 4.5 times higher than that in the AS mouse group, respectively (*$P = 0.048$ and ***$P = 0.00004$), indicating a higher infiltration of both macrophages and neutrophils (Fig. 7, I and J). Furthermore, the H&E-stained images of carotid plaques revealed the higher level of necrotic areas in plaques in AS mice with LPS treatment (figs. S29 and S31). In addition, H&E staining of other major organs post-afterglow imaging did not reveal pathological changes (fig. S32).

Subsequently, we evaluated the accumulation of nanoparticles in the plaques of a spontaneous atherosclerosis model using afterglow imaging. To establish this model, ApoE$^{-/-}$ mice were fed a high-fat diet for 20 weeks. Subsequently, these mice were intravenously administered RANP. Two hours postinjection, the aortas were excised, segmented into four parts (control and segments 1, 2, and 3), and subjected to afterglow imaging (as detailed in fig. S33). The H&E staining was performed on the aortic segments to confirm the induction of atherosclerosis. The H&E staining revealed atherosclerotic
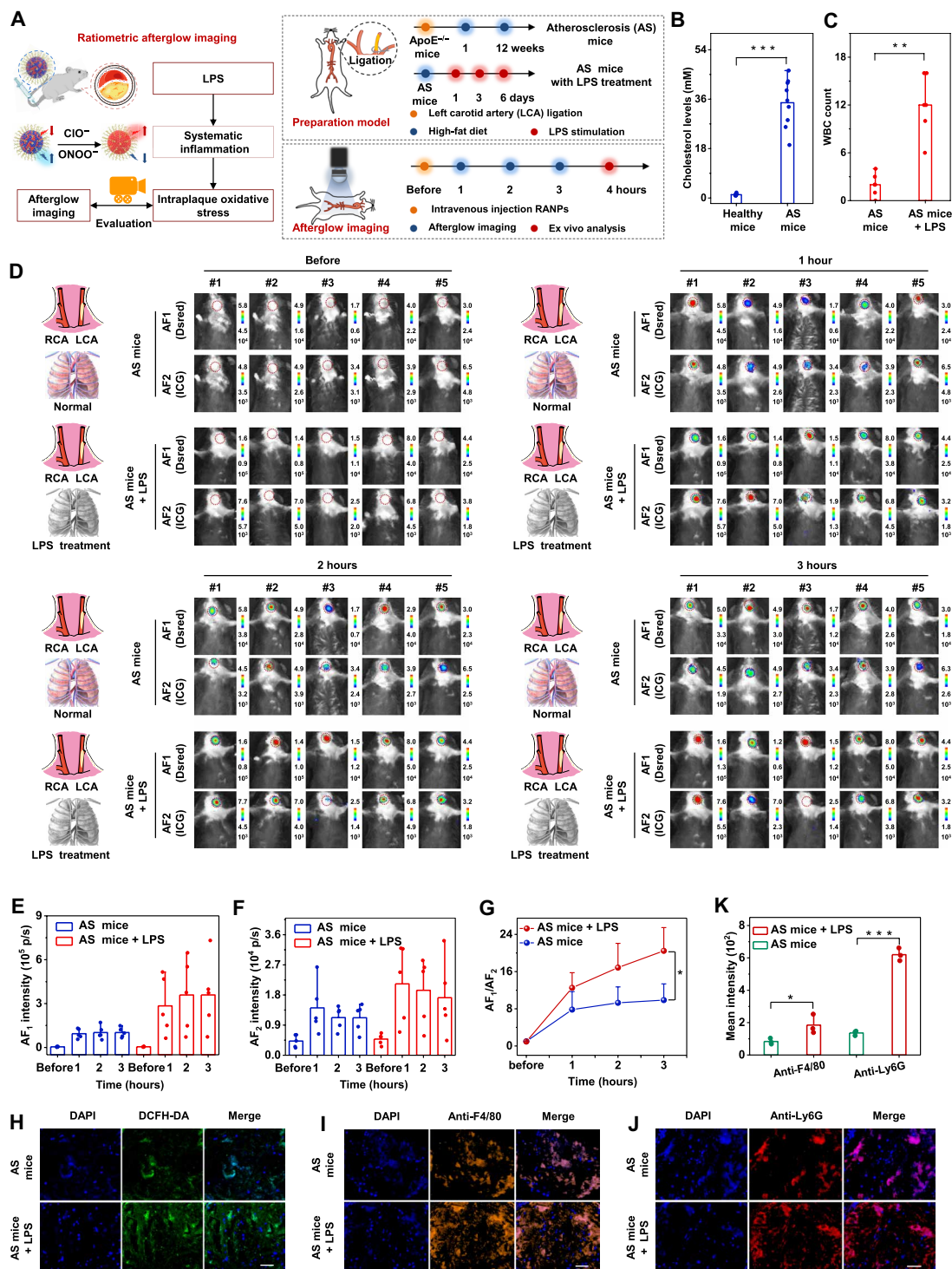
Fig. 7. Afterglow imaging of carotid atherosclerotic mice in vivo and ex vivo. (**A**) Schematic illustration for afterglow imaging of atherosclerotic mice and model preparation. (**B**) The blood cholesterol levels of AS mice and healthy mice ($n = 9$). (**C**) WBC counts of different mice ($n = 5$). (**D**) Afterglow imaging of AS mice and AS mice with LPS treatment before and after injection of RANPs. (**E**) AF1, (**F**) AF2, and (**G**) AF1/AF2 values of AS mice and AS mice with LPS treatment ($n = 5$). (**H**) Fluorescent confocal images of DCFH-DA within the plaque. Scale bar, 50 μm. Fluorescent confocal images of (**I**) macrophage infiltration and (**J**) neutrophil infiltration within the plaque. Scale bars, 50 μm. (**K**) Quantification of intraplaque mean orange fluorescence and red fluorescence intensity in [(I) and (J)], respectively ($n = 3$). Data are shown as mean ± SD (two-tailed Student's t test, *$P < 0.05$, **$P < 0.01$, and ***$P < 0.001$).

plaques in segments 1 through 3, characterized by necrotic cores, while the control segment showed no plaque formation (fig. S33). Further analysis involved measuring the percentage of necrotic area using images from H&E staining. We observed increasing necrotic core percentages from segments 1 to 3 (fig. S33). Afterglow imaging was used to assess nanoparticle accumulation in the aortic segments. The ratio of afterglow signals (AF_1/AF_2) increased sequentially from segment 1 to 3, suggesting elevated oxidative stress levels (fig. S34).

Furthermore, macrophage and neutrophil infiltration was assessed using anti-F4/80 and anti-Ly6G staining, respectively. These immunostainings revealed distinct patterns of infiltration that intensified from segment 1 to segment 3, as reflected by increasing mean fluorescence intensities (fig. S35). To further corroborate the increasing oxidative stress levels, we used DCFH-DA staining, which showed escalating fluorescence intensity across the segments (fig. S36). In addition, the levels of malondialdehyde (MDA) and glutathione (GSH) were quantified to directly assess oxidative stress within the plaques. Results from MDA and GSH assays indicated an increase in MDA and a decrease in GSH across the aortic segments, confirming the trend of increasing oxidative stress (fig. S37).

DISCUSSION

Here, we introduced difuranfluoreno-dithiophen–based polymers to achieve the ultrabright afterglow luminescence, ultralow-power excitation, ultrashort acquisition time, and negligible photobleaching for high-sensitivity, lossless, and longitudinal molecular imaging in vivo. To enhance afterglow luminescence beyond previous reports, we used a molecular engineering strategy to rationally regulate molecular structures of polymer. Specifically, we incorporated fluoro-quinoxaline, Qx, and benzotriazole for modulating the electron-donating ability of the "acceptors (A) unit" of polymers, so as to systematically control the ROS production capability, ROS capturing capability, and fluorescence QY of polymer and further improve afterglow luminescence.

We synthesized four kinds of polymers by linking different dithiophene-substituted "A units" and furan-fused fluorene "D units." Notably, A4-NPs that incorporated dithiophene-substituted benzotriazole unit and furan-fused fluorene unit had the high efficacy in producing and capturing ROS, as well as in luminescent intensity. Consequently, 576-fold, 55-fold, and 260-fold enhancements of afterglow luminescence intensity of A4-NPs were achieved compared to A1-NPs, A2-NPs, and A3-NPs, respectively. Moreover, A4-NPs showed approximately 130-fold higher afterglow luminescence intensity than the commonly used afterglow polymer (MEHPPV). Thereby, the A4-NPs achieved ultralow-power light excitation (0.087 mW/cm^2) and ultrashort acquisition time (down to 0.01 s). In addition, the enhanced excitation efficiency allowed A4-NPs to be reexcited more than 20 cycles with no observable photobleaching.

Furthermore, we developed RANPs by doping A4-NPs with the ORM for accurate quantification of ClO^- or $ONOO^-$ via the ratio of two emissions (AF_1/AF_2). RANPs could target the plaque of mice and detect levels of oxidative stress within plaques. Moreover, the ratiometric afterglow signals were positively correlated with intraplaque macrophage infiltration, neutrophil infiltration, and necrotic percentage. As such, this innovative approach provides a tool for cardiovascular imaging and diagnostics, which is conducive to the auxiliary diagnosis and risk stratification of atherosclerotic plaques.

Despite the molecular engineering strategy that has enabled the development of ultrabright afterglow luminescence for ratiometric afterglow imaging of intraplaque oxidative stress, several drawbacks remain that necessitate further investigation. First, the ratiometric signal variation of RANPs within atherosclerotic plaques is relatively modest, potentially compromising the sensitivity of the imaging modality. This limitation can be mitigated by the development of more sensitive and specific probes tailored to diverse biological targets. Second, while afterglow imaging avoids the interference of autofluorescence, the reliance on light as an excitation source is constrained by its limited penetration depth. This presents a challenge in the context of imaging deep disease model. To address this, the exploration and development of ultrasonic imaging techniques are warranted, as they offer the capability to visualize deep tissue structures. Last, ROS are widely used as biomarkers for assessing oxidative stress levels in inflammatory diseases. However, the reliance on ROS as a biomarker for certain diseases may be affected by factors such as diet, physical activity, and aging, which induce variations in ROS levels. Consequently, there is a pressing need for further research aimed at developing more reliable diagnostic methodologies capable of detecting disease-specific biomarkers, such as proteases, for enhancing the precise the efficacy of disease diagnosis like atherosclerosis.

MATERIALS AND METHODS
Synthesis and afterglow performance testing of nanoparticles
Preparation of A1-NPs, A2-NPs, A3-NPs, and A4-NPs
For the synthesis of various nanoparticles, a solution of A1, A2, A3, or A4 polymer (0.2 mg) and pluronic-F127 (2.5 mg) in THF (1 ml) was rapidly injected into 9 ml of ultrapure water, followed by sonication for 2 min. Additional sonication for 10 min was performed before the solution was concentrated to 0.2 mg/ml (polymer mass basis) using ultrafiltration (100,000 molecular weight cutoff, 4000 rpm) after removing excess THF via rotary evaporation at 45°C. The solution was then stored in the dark at approximately 4°C.
Spectroscopic measurements
Absorption and fluorescence spectra in solution were recorded using absorption spectrometry and a spectrofluorometer FS5, respectively. Polymer solutions in THF (3 μg/ml, 200 μl) for A1, A2, A3, or A4 and nanoparticle solutions (10 μg/ml, 200 μl) for polymer-based nanoparticles were prepared for these measurements.
Afterglow luminescence of A1-NPs, A2-NPs, A3-NPs, and A4-NPs
To assess the afterglow intensity of various polymer nanoparticles, samples including A1-NPs, A2-NPs, A3-NPs, and A4-NPs (50 μg/ml, 10 μl) were distributed into polymerase chain reaction tubes and then preirradiated with white light (12 mW/cm^2) for 20 s. The afterglow luminescence was conducted using the IVIS Lumina XR imaging system, operating under bioluminescence (without excitation). The imaging parameters for afterglow luminescence included an open filter setting, an acquisition time of 30 s, and a field of view set to C. Afterglow luminescence images underwent region of interest analysis via Living Image 4.0 Software.

Afterglow imaging of atherosclerotic mice in vivo and ex vivo
Preparation of carotid atherosclerotic models
All animal experiments were conducted in strict accordance with relevant laws and institutional guidelines, receiving approval from the Institutional Animal Care and Use Committee of Hunan University

[protocol number: SYXK (xiang) 2022-0007]. Female BALB/c and male C57 mice were procured from Hunan Slake Jingda Laboratory Animal Co. Ltd., while ApoE$^{-/-}$ male mice were sourced from Gem-Pharmatech Co. Ltd.

For establishment of arteriosclerosis (AS) mouse models, the left carotid artery of ApoE$^{-/-}$ male mice (8 weeks) was surgically ligated. Then, male mice were fed with high-fat diet for 12 weeks to obtain carotid atherosclerotic mice. For establishment of AS mice with the LPS treatment model, the carotid atherosclerotic mice were intranasally instilled with LPS (2 mg/ml, 25 µl) once every 3 days (three times).

Measuring the blood cholesterol levels

Blood cholesterol levels were measured in AS model mice and compared to healthy C57 male mice. Blood samples were centrifuged at 2200 rpm for 15 min to obtain serum, which was analyzed for cholesterol levels using a total cholesterol detection kit.

Measuring WBC

WBC counts were performed on blood samples from healthy mice, plaque-bearing mice, and plaque-bearing mice with LPS treatment. Cell smears were analyzed under a fluorescent inverted microscope, with the number of WBCs counted in each field of view.

Afterglow imaging of AS mice and AS mice with LPS treatment

For in vivo afterglow imaging, mice were divided into two groups ($n = 5$): (i) AS mice and (ii) AS mice with LPS treatment. Both groups were intravenously injected with RANPs (2.0 mg/ml, 200 µl) containing 5% ORM and then irradiated with white light (30 mW/cm^2, 20 s) on the left carotid artery, while the right carotid artery was shielded. Afterglow images were captured at different time points (1, 2, and 3 hours) using Dsred (AF$_1$) or ICG (AF$_2$) channels.

H&E staining of carotid artery

Carotid arteries were harvested from atherosclerotic mice and immediately embedded in optimal cutting temperature (OCT) compound, followed by rapid freezing at $-80°$C for 30 min. Subsequently, the samples were sectioned to a thickness of 15 µm.

For H&E staining, carotid artery sections were first stained with hematoxylin (10 µl) for 5 min at room temperature, followed by rinsing thrice with ultrapure water. Eosin (10 µl) was then applied for 10 s. After dehydration through three times with ethanol (10%), a drop of neutral balsam was added. Sections were then coverslipped and imaged using a digital slice scanning system. The necrotic core area was quantified by dividing its area by the total plaque size, with calculations performed using ImageJ.

Immunofluorescence staining of carotid artery

For DCFH-DA staining, carotid artery sections were rinsed with ultrapure water twice before incubation with DCFH-DA (10 µM) at 37°C for 60 min. After a secondary rinse with ultrapure water, the sections were labeled with 4′,6-diamidino-2-phenylindole (DAPI) for 10 min at 37°C. Immunofluorescence imaging was then conducted using a laser confocal microscope.

Macrophage detection involved rinsing the artery sections twice with ultrapure water, followed by incubation with F4/80 antibody (1:500; Bio-Rad, MCA497GA) for 60 min at 37°C. After three rinses with deionized water, sections were incubated with a fluorescein isothiocyanate (FITC)–labeled secondary antibody applied for 10 min at 37°C for nuclear staining, before proceeding to immunofluorescence imaging on a laser confocal microscope.

Neutrophil staining required a similar protocol, where sections were first rinsed and then incubated with a FITC anti-mouse Ly6G antibody (1:200; BioLegend, 127605) for 60 min at 37°C. Following

two rinses, sections were stained with DAPI (10 µM) for 10 min at 37°C, with immunofluorescence imaging performed on a laser confocal microscope. Immunofluorescence imaging used a Nikon Confocal Microscopy, with DCFH-DA excited at 488 nm, both the anti-F4/80 and directly labeled anti-Ly6G antibodies also excited at 488 nm, and DAPI at an excitation wavelength of 405 nm.

Preparation of spontaneous atherosclerosis model

To induce spontaneous atherosclerosis in mice, the ApoE$^{-/-}$ mice (8 weeks) were fed with the high-fat diet for 20 weeks.

The accumulation of RANP in spontaneous atherosclerosis model

To evaluate the accumulation of RANP in spontaneous atherosclerosis model, we measured the afterglow signal of the aorta. The mice were intravenously injected with RANP (3.0 mg/ml, 200 µl). Two hours postinjection, the aorta was excised, segmented into four parts (control and segments 1, 2, and 3), and subjected to afterglow imaging. Subsequently irradiated with white light (30 mW/cm^2) for 20 s, the afterglow images were recorded at Dsred (AF1) or ICG (AF2) channels using the IVIS imaging system operating under bioluminescence (without excitation).

The H&E staining of different segments (control and segments 1, 2, and 3)

Each segment of aorta was harvested from atherosclerotic mice and immediately embedded in OCT compound, followed by rapid freezing at $-80°$C for 30 min. Subsequently, the samples were sectioned to a thickness of 15 µm.

For H&E staining, the aortic slices of each segment were stained with hematoxylin (10 µl) for 5 min at room temperature, and then those slices were rinsed three times with ultrapure water and stained with eosin (10 µl) for 10 s. Next, those slices were dehydrated three times with 10% ethanol and added one drop of neutral balsam. Last, those slices were covered with a coverslip and scanned by the Digital Slice Scanning System. The proportion of the necrotic core relative to the total plaque area was quantitatively assessed using ImageJ software.

Immunofluorescence staining of different segments (segments 1, 2, and 3)

For macrophage staining experiment, the aortic slices of each segment were rinsed with ultrapure water and incubated with a F4/80 primary antibody (1:500; Bio-Rad, MCA497GA) for 60 min at 37°C. Following this, the slices were rinsed again with ultrapure water, incubated with a FITC-labeled secondary antibody for 60 min at 37°C, and then labeled with DAPI for 10 min. The images of the slices were captured using Nikon Confocal Microscopy with FITC excited at 488 nm and DAPI excited at 405 nm.

For neutrophil staining experiment, the aortic slices of each segment were rinsed with ultrapure water and incubated with a FITC anti-mouse Ly6G antibody (1:200; BioLegend, 127605) for 60 min at 37°C. Following this, the slices were rinsed again with ultrapure water and labeled with DAPI for 10 min. The images of the slices were captured using Nikon Confocal Microscopy with anti-Ly6G antibodies excited at 488 nm and DAPI excited at 405 nm.

For DCFH-DA staining, the aortic slices of each segment were rinsed with ultrapure water twice before incubation with DCFH-DA (10 µM) for 60 min at 37°C. After a secondary rinse with ultrapure water, the slices were labeled with DAPI for 10 min at 37°C. Immunofluorescence imaging was then conducted using a laser confocal microscope with DCFH-DA excited at 488 nm and DAPI excited at 405 nm.

MDA and GSH content measuring of different segments (segments 1, 2, and 3)

The collected aorta of different regions was prepared respectively into a 10% homogenate solutions. The homogenate was centrifuged (8000 rpm, 4°C), and then the supernatant was obtained. The MDA and GSH contents of the supernatant were tested respectively using an MDA assay kit (A003-1-2, purchased from Nanjing Jiancheng Bioengineering Institute) and a GSH assay kit (BC1175, purchased from Beijing Solarbio Science and Technology Co. Ltd.) according to the standard protocol.

Statistics and data analysis

Results were expressed as the mean ± SD. Statistical significance was performed by two-tailed Student's t test (*$P < 0.05$, **$P < 0.01$, and ***$P < 0.001$).

Supplementary Materials

This PDF file includes:
Tables S1 to S8
Supplementary Materials and Methods
Figs. S1 to S37
Density functional theory (DFT) calculations
References

REFERENCES AND NOTES

1. R. Beaglehole, D. Yach, Globalisation and the prevention and control of non-communicable disease: The neglected chronic diseases of adults. *Lancet* **362**, 903–908 (2003).
2. P. Song, Z. Fang, H. Wang, Y. Cai, K. Rahimi, Y. Zhu, F. G. R. Fowkes, F. J. I. Fowkes, I. Rudan, Global and regional prevalence, burden, and risk factors for carotid atherosclerosis: A systematic review, meta-analysis, and modelling study. *Lancet Glob. Health* **8**, e721–e729 (2020).
3. J. M. Farina, K. Liblik, P. Iomini, A. F. Miranda-Arboleda, C. Saldarriaga, I. Mendoza, E. J. Zaidel, J. M. Rubio-Campal, A. Sosa-Liprandi, A. Baranchuk, Infections and cardiovascular disease: JACC focus seminar 1/4. *J. Am. Coll. Cardiol.* **81**, 71–80 (2023).
4. S. E. Engelen, A. J. B. Robinson, Y.-X. Zurke, C. Monaco, Therapeutic strategies targeting inflammation and immunity in atherosclerosis: How to proceed? *Nat. Rev. Cardiol.* **19**, 522–542 (2022).
5. J. Deguchi, M. Aikawa, C.-H. Tung, E. Aikawa, D.-E. Kim, V. Ntziachristos, R. Weissleder, P. Libby, Inflammation in atherosclerosis. *Circulation* **114**, 55–62 (2006).
6. W. J. Hucker, F. A. Jaffer, ^{18}F-FDG PET imaging of atherosclerosis—A new approach to detect inflamed, high-risk coronary plaques? *Curr. Cardiovasc. Imaging Rep.* **4**, 1–3 (2011).
7. P. M. Ridker, Inflammation, infection, and cardiovascular risk: How good is the clinical evidence? *Circulation* **97**, 1671–1674 (1998).
8. J. Hettwer, J. Hinterdobler, B. Miritsch, M.-A. Deutsch, X. Li, C. Mauersberger, A. Moggio, Q. Braster, H. Gram, A. A. B. Robertson, M. A. Cooper, O. Groß, M. Krane, C. Weber, W. Koenig, O. Soehnlein, N. H. Adamstein, P. Ridker, H. Schunkert, P. Libby, T. Kessler, H. B. Sager, Interleukin-1β suppression dampens inflammatory leucocyte production and uptake in atherosclerosis. *Cardiovasc. Res.* **118**, 2778–2791 (2021).
9. Y. Qiao, M. Etesami, S. Malhotra, B. C. Astor, R. Virmani, F. D. Kolodgie, H. H. Trout III, B. A. Wasserman, Identification of intraplaque hemorrhage on MR angiography images: A comparison of contrast-enhanced mask and time-of-flight techniques. *AJNR Am. J. Neuroradiol.* **32**, 454–459 (2011).
10. C. Collet, E. Conte, S. Mushtaq, S. Brouwers, T. Shinke, A. U. Coskun, Z. Pu, D. Hakim, P. H. Stone, D. Andreini, Reviewing imaging modalities for the assessment of plaque erosion. *Atherosclerosis* **318**, 52–59 (2021).
11. L. Zhang, X. Ii, Q. Lyu, G. Shi, Imaging diagnosis and research progress of carotid plaque vulnerability. *J. Clin. Ultrasound* **50**, 905–912 (2022).
12. J. W. Verjans, E. A. Osborn, G. J. Ughi, M. A. Calfon Press, E. Hamidi, A. P. Antoniadis, M. I. Papafaklis, M. F. Conrad, P. Libby, P. H. Stone, R. P. Cambria, G. J. Tearney, F. A. Jaffer, Targeted near-infrared fluorescence imaging of atherosclerosis: Clinical and intracoronary evaluation of indocyanine green. *JACC Cardiovasc. Imaging* **9**, 1087–1095 (2016).
13. K. Wang, H. Gao, Y. Zhang, H. Yan, J. Si, X. Mi, S. Xia, X. Feng, D. Liu, D. Kong, T. Wang, D. Ding, Highly bright AIE nanoparticles by regulating the substituent of rhodanine for precise early detection of atherosclerosis and drug screening. *Adv. Mater.* **34**, 2106994 (2022).
14. J. W. Song, J. W. Ahn, M. W. Lee, H. J. Kim, D. O. Kang, R. H. Kim, U. G. Kang, Y. H. Kim, J. Han, Y. H. Park, H. S. Nam, H. Yoo, K. Park, J. W. Kim, Targeted theranostic photoactivation on atherosclerosis. *J. Nanobiotechnology* **19**, 338 (2021).
15. Z. Ye, M. Ji, K. Wu, J. Yang, A.-A. Liu, W. Sun, D. Ding, D. Liu, In-sequence high-specificity dual-reporter unlocking of fluorescent probe enables the precise identification of atherosclerotic plaques. *Angew. Chem. Int. Ed.* **61**, 202204518 (2022).
16. H. Qiao, Y. Wang, R. Zhang, Q. Gao, X. Liang, L. Gao, Z. Jiang, R. Qiao, D. Han, Y. Zhang, Y. Qiu, J. Tian, M. Gao, F. Cao, MRI/optical dual-modality imaging of vulnerable atherosclerotic plaque with an osteopontin-targeted probe based on Fe_3O_4 nanoparticles. *Biomaterials* **112**, 336–345 (2017).
17. H. Kim, S. Kumar, D.-W. Kang, H. Jo, J.-H. Park, Affinity-driven design of cargo-switching nanoparticles to leverage a cholesterol-rich microenvironment for atherosclerosis therapy. *ACS Nano* **14**, 6519–6531 (2020).
18. F. Chen, J. Chen, C. Han, Z. Yang, T. Deng, Y. Zhao, T. Zheng, X. Gan, C. Yu, Theranostics of atherosclerosis by the indole molecule-templated self-assembly of probucol nanoparticles. *J. Mater. Chem. B* **9**, 4134–4142 (2021).
19. L. Xu, Z. Li, Y. Ma, L. Lei, R. Yue, H. Cao, S. Huan, W. Sun, G. Song, Imaging carotid plaque burden in living mice via hybrid semiconducting polymer nanoparticles-based near-infrared-II fluorescence and magnetic resonance imaging. *Research* **6**, 0186 (2023).
20. Q. Wu, W. Pan, G. Wu, F. Wu, Y. Guo, X. Zhang, CD40-targeting magnetic nanoparticles for MRI/optical dual-modality molecular imaging of vulnerable atherosclerotic plaques. *Atherosclerosis* **369**, 17–26 (2023).
21. Y. Zhang, J. Li, J. Zhao, X. Li, Z. Wang, Y. Huang, H. Zhang, Q. Liu, Y. Lei, D. Ding, π–π interaction-induced organic long-wavelength room-temperature phosphorescence for in vivo atherosclerotic plaque imaging. *Angew. Chem. Int. Ed.* **63**, e202313890 (2024).
22. Y. Liu, L. Teng, X.-F. Lou, X.-B. Zhang, G. Song, "Four-in-one" design of a hemicyanine-based modular scaffold for high-contrast activatable molecular afterglow imaging. *J. Am. Chem. Soc.* **145**, 5134–5144 (2023).
23. Y. Liu, L. Teng, Y. Lyu, G. Song, X.-B. Zhang, W. Tan, Ratiometric afterglow luminescent nanoplatform enables reliable quantification and molecular imaging. *Nat. Commun.* **13**, 2216 (2022).
24. Q. Miao, C. Xie, X. Zhen, Y. Lyu, H. Duan, X. Liu, J. V. Jokerst, K. Pu, Molecular afterglow imaging with bright, biodegradable polymer nanoparticles. *Nat. Biotechnol.* **35**, 1102–1110 (2017).
25. Y. Lyu, D. Cui, J. Huang, W. Fan, Y. Miao, K. Pu, Near-infrared afterglow semiconducting nano-polycomplexes for the multiplex differentiation of cancer exosomes. *Angew. Chem. Int. Ed.* **58**, 4983–4987 (2019).
26. S. Liao, Y. Wang, Z. Li, Y. Zhang, X. Yin, S. Huan, X.-B. Zhang, S. Liu, G. Song, A novel afterglow nanoreporter for monitoring cancer therapy. *Theranostics* **12**, 6883–6897 (2022).
27. J. Li, K. Pu, Development of organic semiconducting materials for deep-tissue optical imaging, phototherapy and photoactivation. *Chem. Soc. Rev.* **48**, 38–71 (2019).
28. W. Chen, Y. Zhang, Q. Li, Y. Jiang, H. Zhou, Y. Liu, Q. Miao, M. Gao, Near-infrared afterglow luminescence of chlorin nanoparticles for ultrasensitive in vivo imaging. *J. Am. Chem. Soc.* **144**, 6719–6726 (2022).
29. W. Huang, W. Zeng, Z. Huang, D. Fang, H. Liu, M. Feng, L. Mao, D. Ye, Ratiometric afterglow luminescent imaging of matrix metalloproteinase-2 activity via an energy diversion process. *Angew. Chem. Int. Ed.* **63**, e202404244 (2024).
30. S. Liu, Y. Tian, D. Ye, Seeing deeper via radio afterglow imaging. *Chem. Biomed. Imaging* **2**, 1–3 (2024).
31. J. Huang, L. Su, C. Xu, X. Ge, R. Zhang, J. Song, K. Pu, Molecular radio afterglow probes for cancer radiodynamic theranostics. *Nat. Mater.* **22**, 1421–1429 (2023).
32. L. Yang, S. Gai, H. Ding, D. Yang, L. Feng, P. Yang, Recent progress in inorganic afterglow materials: Mechanisms, persistent luminescent properties, modulating methods, and bioimaging applications. *Adv. Opt. Mater.* **11**, 2202382 (2022).
33. P. Pei, Y. Chen, C. Sun, Y. Fan, Y. Yang, X. Liu, L. Lu, M. Zhao, H. Zhang, D. Zhao, X. Liu, F. Zhang, X-ray-activated persistent luminescence nanomaterials for NIR-II imaging. *Nat. Nanotechnol.* **16**, 1011–1018 (2021).
34. S. He, C. Xie, Y. Jiang, K. Pu, An organic afterglow protheranostic nanoassembly. *Adv. Mater.* **31**, 1902672 (2019).
35. C. Chen, H. Gao, H. Ou, R. T. K. Kwok, Y. Tang, D. Zheng, D. Ding, Amplification of activated near-infrared afterglow luminescence by introducing twisted molecular geometry for understanding neutrophil-involved diseases. *J. Am. Chem. Soc.* **144**, 3429–3441 (2022).
36. X. Li, C. Yin, S. S. Liew, C.-S. Lee, K. Pu, Organic semiconducting luminophores for near-infrared afterglow, chemiluminescence, and bioluminescence imaging. *Adv. Funct. Mater.* **31**, 2106154 (2021).
37. C. Xu, J. Huang, Y. Jiang, S. He, C. Zhang, K. Pu, Nanoparticles with ultrasound-induced afterglow luminescence for tumour-specific theranostics. *Nat. Biomed. Eng.* **7**, 298–312 (2023).
38. X. Wang, K. Pu, Molecular substrates for the construction of afterglow imaging probes in disease diagnosis and treatment. *Chem. Soc. Rev.* **52**, 4549–4566 (2023).

39. Y. Jiang, K. Pu, Molecular probes for autofluorescence-free optical imaging. *Chem. Rev.* **121**, 13086–13131 (2021).

40. L. Wu, Y. Ishigaki, Y. Hu, K. Sugimoto, W. Zeng, T. Harimoto, Y. Sun, J. He, T. Suzuki, X. Jiang, H.-Y. Chen, D. Ye, H$_2$S-activatable near-infrared afterglow luminescent probes for sensitive molecular imaging in vivo. *Nat. Commun.* **11**, 446 (2020).

41. J. Li, G.-Q. Zhang, Y. Zhang, Y. Tang, D. Ding, W. Li, Q. Liu, Building highly light-harvesting near-infrared AIEgens using triazole-based luminescent core for improved intravital afterglow imaging. *Adv. Funct. Mater.* **33**, 2212380 (2023).

42. Q. Tian, M. Tang, Y. Sun, R. Zou, Z. Chen, M. Zhu, S. Yang, J. Wang, J. Wang, J. Hu, Hydrophilic flower-like CuS superstructures as an efficient 980 nm laser-driven photothermal agent for ablation of cancer cells. *Adv. Mater.* **23**, 3542–3547 (2011).

43. Y. Fan, S. Liu, M. Wu, L. Xiao, Y. Fan, M. Han, K. Chang, Y. Zhang, X. Zhen, Q. Li, Z. Li, Mobile phone flashlight-excited red afterglow bioimaging. *Adv. Mater.* **34**, 2201280 (2022).

44. L. Yang, M. Zhao, W. Chen, J. Zhu, W. Xu, Q. Li, K. Pu, Q. Miao, A highly bright near-infrared afterglow luminophore for activatable ultrasensitive in vivo imaging. *Angew. Chem. Int. Ed. Engl.* **63**, e202313117 (2024).

45. Z. Li, L. Xu, J.-Y. Li, L. Lei, P.-Z. Liang, Q. Wu, F. Yang, T.-B. Ren, X. Yin, L. Yuan, X.-B. Zhang, Superoxide anion-mediated afterglow mechanism-based water-soluble zwitterion dye achieving renal-failure mice detection. *J. Am. Chem. Soc.* **145**, 26736–26746 (2023).

46. L. Lei, F. Yang, X. Meng, L. Xu, P. Liang, Y. Ma, Z. Dong, Y. Wang, X.-B. Zhang, G. Song, Noninvasive imaging of tumor glycolysis and chemotherapeutic resistance via de novo design of molecular afterglow scaffold. *J. Am. Chem. Soc.* **145**, 24386–24400 (2023).

47. L. Chen, K. Sun, D. Hu, X. Su, L. Guo, J. Yin, Y. Pei, Y. Fan, Q. Liu, M. Xu, W. Feng, F. Li, Ultra-long near-infrared repeatable photochemical afterglow mediated by reversible storage of singlet oxygen for information encryption. *Angew. Chem.* **135**, e202218670 (2023).

48. Y. Li, D. He, Q. Zheng, R. Tang, Q. Wan, B. Z. Tang, Z. Wang, Single-component photochemical afterglow near-infrared luminescent nano-photosensitizers: Bioimaging and photodynamic therapy. *Adv. Healthc. Mater.* **13**, 2304392 (2024).

49. Y. Jiang, M. Zhao, J. Miao, W. Chen, Y. Zhang, M. Miao, L. Yang, Q. Li, Q. Miao, Acidity-activatable upconversion afterglow luminescence cocktail nanoparticles for ultrasensitive in vivo imaging. *Nat. Commun.* **15**, 2124 (2024).

50. J. Zhu, W. Chen, L. Yang, Y. Zhang, B. Cheng, W. Gu, Q. Li, Q. Miao, A self-sustaining near-infrared afterglow chemiluminophore for high-contrast activatable imaging. *Angew. Chem. Int. Ed.* **63**, e202318545 (2024).

51. X. Wang, H. Chen, J. Yuan, Q. Wei, J. Li, L. Jiang, J. Huang, Y. Li, Y. Li, Y. Zou, Precise fluorination of polymeric donors towards efficient non-fullerene organic solar cells with balanced open circuit voltage, short circuit current and fill factor. *J. Mater. Chem. A* **9**, 14752–14757 (2021).

52. Y. Jiang, J. Huang, X. Zhen, Z. Zeng, J. Li, C. Xie, Q. Miao, J. Chen, P. Chen, K. Pu, A generic approach towards afterglow luminescent nanoparticles for ultrasensitive in vivo imaging. *Nat. Commun.* **10**, 2064 (2019).

53. H. Zhu, I. Badía-Domínguez, B. Shi, Q. Li, P. Wei, H. Xing, M. C. Ruiz Delgado, F. Huang, Cyclization-promoted ultralong low-temperature phosphorescence via boosting intersystem crossing. *J. Am. Chem. Soc.* **143**, 2164–2169 (2021).

54. Z. Hou, Y. Zhang, K. Deng, Y. Chen, X. Li, X. Deng, Z. Cheng, H. Lian, C. Li, J. Lin, UV-emitting upconversion-based TiO$_2$ photosensitizing nanoplatform: Near-infrared light mediated in vivo photodynamic therapy via mitochondria-involved apoptosis pathway. *ACS Nano* **9**, 2584–2599 (2015).

55. Y.-C. Chen, Y.-T. Li, C.-L. Lee, Y.-T. Kuo, C.-L. Ho, W.-C. Lin, M.-C. Hsu, X. Long, J.-S. Chen, W.-P. Li, C.-H. Su, A. Okamoto, C.-S. Yeh, Electroactive membrane fusion-liposome for increased electron transfer to enhance radiodynamic therapy. *Nat. Nanotechnol.* **18**, 1492–1501 (2023).

56. Y. Wang, G. Song, S. Liao, Q. Qin, Y. Zhao, L. Shi, K. Guan, X. Gong, P. Wang, X. Yin, Q. Chen, X.-B. Zhang, Cyclic amplification of the afterglow luminescent nanoreporter enables the prediction of anti-cancer efficiency. *Angew. Chem. Int. Ed.* **60**, 19779–19789 (2021).

57. L. Lu, T. Zheng, Q. Wu, A. M. Schneider, D. Zhao, L. Yu, Recent advances in bulk heterojunction polymer solar cells. *Chem. Rev.* **115**, 12666–12731 (2015).

58. Y. Zhang, J. Sun, Y. Sun, Y. Tang, R. Wang, Mechanistic and kinetic study on the reaction of thiophene with hydroxyl radical. *Comput. Theor. Chem.* **1092**, 74–81 (2016).

59. P. Xie, C. Xue, J. Luo, S. Shi, D. Du, Decatungstate-mediated solar photooxidative cleavage of C=C bonds using air as an oxidant in water. *Green Chem.* **23**, 5936–5943 (2021).

60. W. Fudickar, T. Linker, Why triple bonds protect acenes from oxidation and decomposition. *J. Am. Chem. Soc.* **134**, 15071–15082 (2012).

61. C. Lu, C. Zhang, P. Wang, Y. Zhao, Y. Yang, Y. Wang, H. Yuan, S. Qu, X. Zhang, G. Song, K. Pu, Light-free generation of singlet oxygen through manganese-thiophene nanosystems for pH-responsive chemiluminescence imaging and tumor therapy. *Chem* **6**, 2314–2334 (2020).

62. R. F. Kubin, A. N. Fletcher, Fluorescence quantum yields of some rhodamine dyes. *J. Lumin.* **27**, 455–462 (1982).

63. K. Hanaoka, S. Iwaki, K. Yagi, T. Myochin, T. Ikeno, H. Ohno, E. Sasaki, T. Komatsu, T. Ueno, M. Uchigashima, T. Mikuni, K. Tainaka, S. Tahara, S. Takeuchi, T. Tahara, M. Uchiyama,
T. Nagano, Y. Urano, General design strategy to precisely control the emission of fluorophores via a twisted intramolecular charge transfer (TICT) process. *J. Am. Chem. Soc.* **144**, 19778–19790 (2022).

64. R. Bazaz, H. M. Marriott, C. Wright, J. Chamberlain, L. E. West, C. Gelsthorpe, P. R. Heath, A. Maleki-Dizaji, S. E. Francis, D. H. Dockrell, Transient increase in atherosclerotic plaque macrophage content following *Streptococcus pneumoniae* pneumonia in ApoE-deficient mice. *Front. Cell. Infect. Microbiol.* **13**, 1090550 (2023).

65. Y. Wang, W. Wang, N. Wang, A. R. Tall, I. Tabas, Mitochondrial oxidative stress promotes atherosclerosis and neutrophil extracellular traps in aged mice. *Arterioscler. Thromb. Vasc. Biol.* **37**, e99–e107 (2017).

66. R. A. Grant, L. Morales-Nebreda, N. S. Markov, S. Swaminathan, M. Querrey, E. R. Guzman, D. A. Abbott, H. K. Donnelly, A. Donayre, I. A. Goldberg, Z. M. Klug, N. Borkowski, Z. Lu, H. Kihshen, Y. Politanska, L. Sichizya, M. Kang, A. Shilatifard, C. Qi, J. W. Lomasney, A. C. Argento, J. M. Kruser, E. S. Malsin, C. O. Pickens, S. B. Smith, J. M. Walter, A. E. Pawlowski, D. Schneider, P. Nannapaneni, H. Abdala-Valencia, A. Bharat, C. J. Gottardi, G. R. S. Budinger, A. V. Misharin, B. D. Singer, R. G. Wunderink, NU SCRIPT Study Investigators, Circuits between infected macrophages and T cells in SARS-CoV-2 pneumonia. *Nature* **590**, 635–641 (2021).

67. U. Förstermann, N. Xia, H. Li, Roles of vascular oxidative stress and nitric oxide in the pathogenesis of atherosclerosis. *Circ. Res.* **120**, 713–735 (2017).

68. W. James, M. D. Leatherman, F. Alfred, M. D. Michael, A. Bruce, M. D. Schwartz, R. John, M. D. Hoidal, Lung T cells in hypersensitivity pneumonitis. *Ann. Intern. Med.* **100**, 390–392 (1984).

69. C. Silvestre-Roig, Q. Braster, A. Ortega-Gomez, O. Soehnlein, Neutrophils as regulators of cardiovascular inflammation. *Nat. Rev. Cardiol.* **17**, 327–340 (2020).

70. M. Sang, Y. Huang, L. Wang, L. Chen, Nawsherwan, G. Li, Y. Wang, X. Yu, C. Dai, J. Zheng, An "AND" molecular logic gate as a super-enhancers for de novo designing activatable probe and its application in atherosclerosis imaging. *Adv. Sci.* **10**, 2207066 (2023).

71. M. Sang, Y. Huang, Z. Liu, G. Li, Y. Wang, Z. Yuan, C. Dai, J. Zheng, Peroxynitrite/lipid droplet sequence-activated dual-lock fluorescent probes enable precise intraoperative imaging of atherosclerotic plaques. *ACS Sens.* **8**, 893–903 (2023).

72. M. K. Chung, D. A. Zidar, M. R. Bristow, S. J. Cameron, T. Chan, C. V. Harding, D. H. Kwon, T. Singh, J. C. Tilton, E. J. Tsai, N. R. Tucker, J. Barnard, J. Loscalzo, COVID-19 and cardiovascular disease: From bench to bedside. *Circ. Res.* **128**, 1214–1236 (2021).

73. Y.-Y. Zheng, Y.-T. Ma, J.-Y. Zhang, X. Xie, COVID-19 and the cardiovascular system. *Nat. Rev. Cardiol.* **17**, 259–260 (2020).

74. T. Guo, Y. Fan, M. Chen, X. Wu, L. Zhang, T. He, H. Wang, J. Wan, X. Wang, Z. Lu, Cardiovascular implications of fatal outcomes of patients with coronavirus disease 2019 (COVID-19). *JAMA Cardiol.* **5**, 811–818 (2020).

75. W. J. Hehre, R. Ditchfield, J. A. Pople, Self—Consistent molecular orbital methods. XII. Further extensions of Gaussian—Type basis sets for use in molecular orbital studies of organic molecules. *J. Chem. Phys.* **56**, 2257–2261 (2003).

76. Y. Zhao, D. G. Truhlar, Density functionals with broad applicability in chemistry. *Acc. Chem. Res.* **41**, 157–167 (2008).

77. P. C. Hariharan, J. A. Pople, The influence of polarization functions on molecular orbital hydrogenation energies. *Theor. Chem. Acc.* **28**, 213–222 (1973).

78. R. Ditchfield, W. J. Hehre, J. A. Pople, Self-consistent molecular-orbital methods. IX. An extended Gaussian-type basis for molecular-orbital studies of organic molecules. *J. Chem. Phys.* **54**, 724–728 (2003).

79. M. J. Frisch, J. A. Pople, J. S. Binkley, Self-consistent molecular orbital methods 25. Supplementary functions for Gaussian basis sets. *J. Chem. Phys.* **80**, 3265–3269 (1984).